Holocene activity and seismogenic capability of intraplate thrusts: Insights from the Pampean Ranges, Argentina

Carlos H. Costa[a,*], Lewis A. Owen[b], Walter R. Ricci[a], William J. Johnson[c], Alan D. Halperin[d]

[a] Departamento de Geología, Universidad Nacional de San Luis, E. de los Andes 950, 5700 San Luis, Argentina
[b] Department of Geology, University of Cincinnati, Cincinnati, OH 45221-0013, USA
[c] Rhea Engineers and Consultants, 411 Mars Valencia Road, Valencia, PA 16059, USA
[d] Independent Consultant, Murrysville, PA 15668, USA

ABSTRACT

Trench excavations across the El Molino fault in the southeastern Pampean Ranges of central-western Argentina have revealed a deformation zone composed of opposite-verging thrusts that deform a succession of Holocene sediments. The west-verging thrusts place Precambrian basement over Holocene proximal scarp-derived deposits, whereas the east-verging thrusts form an east-directed fault-propagation fold that deforms colluvium, fluvial and aeolian deposits. Ages for exposed fault-related deposits range from 7.1 ± 0.4 to ~ 0.3 ka. Evidence of surface deformation suggests multiple rupture events with related scarp-derived deposits and a minimum of three surface ruptures younger than 7.1 ± 0.4 ka, the last rupture event being younger than 1 ka. Shortening rates of $\sim 0.7 \pm 0.2$ mm/a are near one order of magnitude higher than those estimated for the faults bounding neighboring crustal blocks and are considered high for this intraplate setting. These ground-rupturing crustal earthquakes are estimated to be of magnitude $M_w \geq 7.0$, a significant discrepancy with the magnitudes $M_w < 6.5$ recorded in the seismic catalog of this region at present with low to moderate seismicity. Results highlight the relevance of identifying primary surface ruptures as well as the seismogenic potential of thrust faults in seemingly stable continental interiors.

1. Introduction

Strong crustal earthquakes (magnitudes > 7) with associated surface deformation have been documented in intraplate settings and continental interiors, but historical records in such regions are generally too short to capture the seismogenic potential and recurrence characteristics of such events (Wesnousky et al., 1984; Crone et al., 1997; Rajendran et al., 2001; McCalpin, 2009; Clark et al., 2014; Grützner et al., 2017; Landgraf et al., 2017). Numerous examples of devastating earthquakes have occurred along faults within these regions that are characterized by low to absent historic seismicity and low to moderate slip rates, as is well illustrated by the 2001 Bhuj, 2005 Kashmir, and 2008 Sichuan earthquakes (McCalpin, 2011). Paleoseismic data are essential for realistic seismic hazard assessments of these regions of ongoing low to moderate seismicity, especially areas where there is an absence of historic seismic surface ruptures.

In particular, compressive tectonic settings represent the most challenging and subtle environments for gathering reliable information about past surface ruptures (Lettis et al., 1997, among others). Data on compressive intraplate tectonic settings are scarce in global databases

as compared with other settings (McCalpin and Carver, 2009; Stirling et al., 2013; Baize et al., 2015). Given the lack of such studies, we examine a low to moderate seismic region of the southeastern Pampean Ranges in central-western Argentina (Fig. 1). Seismic hazard studies in this region have been limited by three main factors: 1) the historical record of earthquakes is < 400 years (INPRES, 1977; www.inpres.gov.ar, accessed 3 March 2018); 2) the lack of primary surface ruptures as evidence of fault source capability; and 3) the difficulty of conducting paleoseismic studies because the recognition of pre-historic earthquakes in the stratigraphic record is hampered by the lack of dateable fine-grained sediment needed to define histories of fault movement.

A natural exposure of a foot-wall shortcut of the uplifted Comechingones Range block near Merlo in the southeastern Pampean Ranges of Argentina (Figs. 1, 2, 3 and 4) led to the first description in this region of Precambrian rocks pushed over Holocene deposits by an east-dipping reverse fault (Costa and Vita Finzi, 1996; Costa et al., 2001). Recent and more complete excavations at this site have revealed a deformation zone that exhibits the interaction of opposite-verging thrusts. Deformed alluvial and colluvial sediments dated by radiocarbon and optically stimulated luminescence (OSL) methods allow a determination of the tectonic
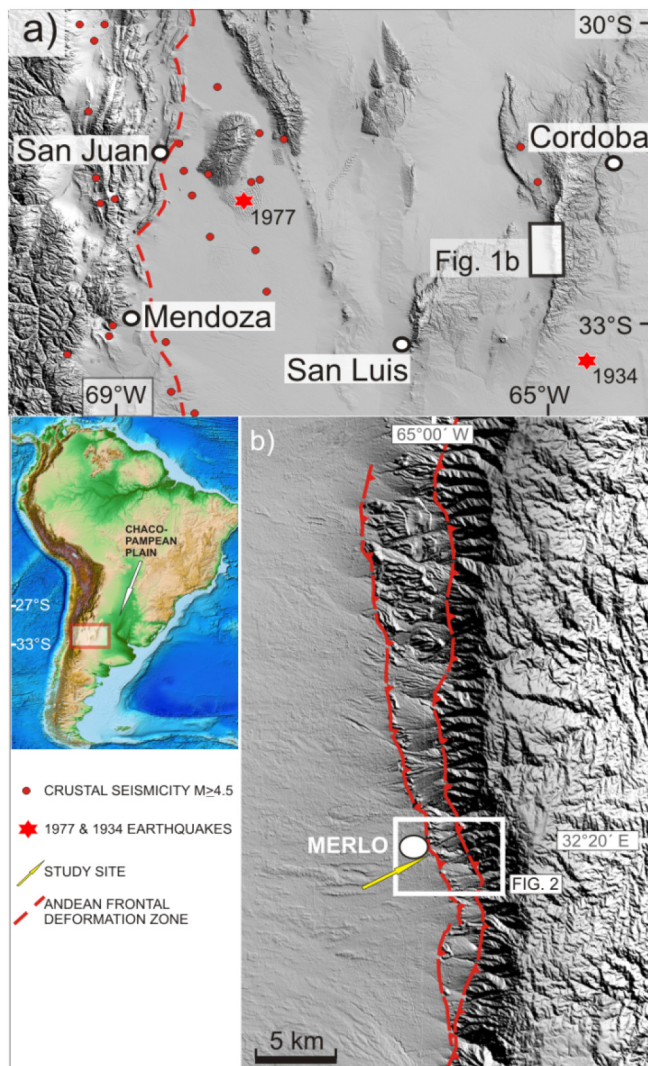
Fig. 1. (a) Regional DEM of the Southern Central Andes and surrounding foreland areas (see inset map for location), covering the southern Pampean Ranges uplifts above the Pampean flat-slab (27–33°S). Red stars indicate the epicenters of the 1977 M_w 7.4 Caucete and the 1934 M_s 6.0 Sampacho earthquakes. (b) Western hillslope of the Comechingones Range where main thrust trace of the Comechingones fault and active Quaternary branch are sketched respectively from east to west. Both structures bound uplifted alluvial deposits defining a piedmont foreland. (For interpretation of the references to color in this figure legend, the reader is referred to the web version of this article.)

evolution during the past ~7 ka. The unusually good preservation of evidence at the study site demonstrates repeated Holocene primary coseismic surface ruptures. Based on other regional considerations, we postulate that the threshold earthquake for rupturing at surface in this region is M > 7. Thus, the documentation of prehistoric primary surface ruptures adds relevant data on fault capability for producing large earthquakes that are not captured by the seismic catalog.

Our results gain more significance considering that the main seismic hazard in Argentina is argued to be concentrated at the Andean piedmont (INPRES, 1977). However, the Pampean Ranges region has several urban areas close to these range-bounding thrusts. Our contribution highlights that the seismic hazard in central Argentina needs to be revisited by incorporating more paleoseismic data. This study also provides insights into intraplate thrust dynamics in areas of ongoing low to moderate seismicity, arguing that some empirical relationships for estimating paleoearthquake magnitude may underestimate the seismic capability of faults in this type of tectonic environment.

2. Tectonic setting

The Pampean Ranges of Argentina constitute the broken foreland of the southern Central Andes that have formed above the Pampean flat-slab subduction segment (27–33°S; Fig. 1a). This region is a modern analog for the uplifts that took place in the Laramide Rocky Mountains that are characterized by mountain blocks bounded by reverse faults and surrounded by basins with flat topography (Jordan et al., 1983; Jordan and Allmendinger, 1986; Ramos et al., 2002).

The last stage of uplift of the Pampean Ranges has been attributed to the shallowing of the Nazca plate at ~8 Ma due to the incorporation of the Juan Férnandez Ridge into the subduction zone (Gutscher et al., 2000; Yáñez et al., 2001, among others). The whole process resulted in a major interplate coupling, crustal shortening and propagation of a deformation wave into the Andean foreland (Ramos, 1988; Yáñez et al., 2001; Ramos et al., 2002). Eastward shifting of magmatism facilitated the foreland fragmentation and uplift of the Pampean Range blocks (Kay et al., 1991; Ramos et al., 2002; Ramos, 2009).

Basement blocks are composed of late Precambrian to early Paleozoic metamorphic and igneous rocks. These blocks exhibit a topographic asymmetry defined by steep-western and gentle-eastern slopes, the latter being characterized by the preservation of remnants of erosional surfaces. This topographic asymmetry is attributed to listric marginal reverse faults (González Bonorino, 1950; Jordan and Allmendinger, 1986), which for most uplifts are usually located at the steeper western hillslopes. The main active Quaternary structures documented in the Pampean Ranges are controlled by inherited structural/lithologic anisotropies, such as boundaries between Paleozoic accreted terranes, Mesozoic continental rift basins and penetrative planar fabrics of the crystalline basement (Schmidt et al., 1995; Ramos et al., 2002; Ramos, 2009; Löbens et al., 2011; Martino et al., 2012, 2016; and Costa et al., 2014, among others).

Crustal earthquakes estimated to be $M_s \leq 6.5$ characterize the background seismicity in this region (INPRES, 1977; Richardson et al., 2012) (Fig. 1a). Evidence of prehistoric earthquakes have been reported along faults in the Pampean Ranges, accounting for primary surface ruptures, large rock avalanches and paleoliquefaction (Costa and Vita Finzi, 1996; Costa, 1999; Hermanns and Strecker, 1999; Costa et al., 2001; González Díaz et al., 1997, 1998; Sagripanti and Villalba, 2009, 2011; Penna et al., 2016). These phenomena have no historical analogs in the region and bear witness to the occurrence of crustal-scale prehistoric earthquakes that are larger and more numerous than would be indicated by the historic record.

3. El Molino fault section

The north-trending Comechingones fault limits the western slope of the Comechingones Range for ~160 km in the south-eastern Pampean Ranges and constitutes the neotectonic uplift front of this block (Figs. 1b and 2) (Costa and Vita Finzi, 1996; Costa et al., 1998, 2001, 2014). The youngest activity associated with this range-bounding fault is argued to have been transferred basin-forward to the El Molino fault splay (Costa, 1996; Costa and Vita Finzi, 1996; Costa et al., 2001), as also documented in other thrust-bounded mountain fronts (Ikeda, 1983; Walker et al., 2003; Thompson et al., 2015). Field surveys along the Comechingones range front have demonstrated that active Quaternary faults are located at the western margin of a foreberg or piedmont foreland (*sensu* Bull, 2007) made up of older alluvial surfaces and cored by basement rocks (Costa, 1996; Costa and Vita Finzi, 1996; Costa et al., 2001) (Figs. 2 and 3). Active Quaternary structures exhibit the same strike and dip as the main thrust trace and are interpreted to be a footwall shortcut of the main Comechingones fault (Costa, 1996; Costa et al., 1998) (Fig. 3). Old alluvial surfaces on the piedmont foreland (Q₃) are back-tilted towards the east, resembling the structural style of the main range block and attesting to the Quaternary activity of the El Molino fault (Figs. 2 and 4a).
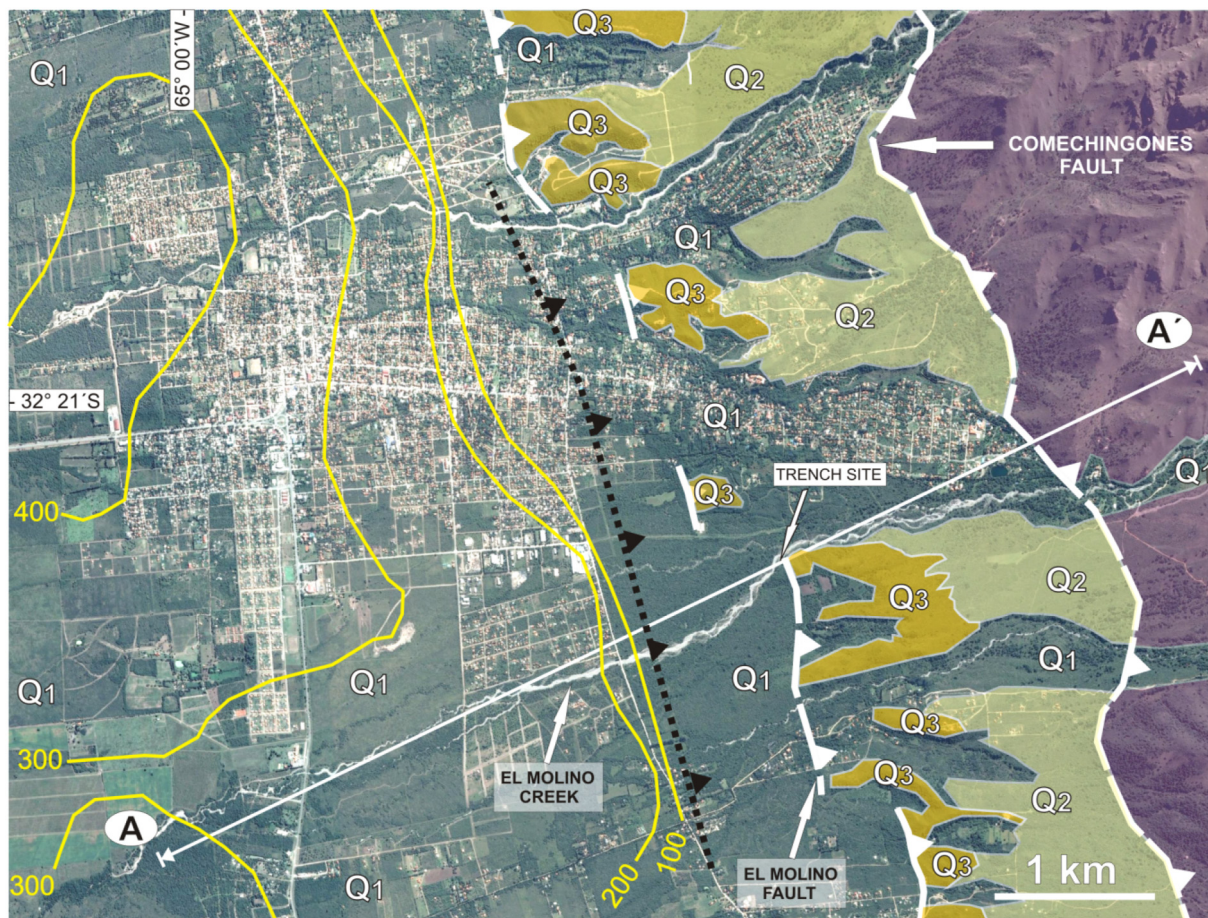
Fig. 2. Google Earth image of the Merlo village area (see Fig. 1b for location). A-A′ corresponds to the cross-section shown in Fig. 3. White dashed lines show from east to west the main Comechingones fault and the El Molino fault section of the active foot-wall shortcut. Black dotted line displays an inferred blind thrust. Most representative Quaternary morphostratigraphic units (mainly alluvial gravels) are distinguished from old (Q_3) to young (Q_1). Yellow solid contour lines represent the thickness of sedimentary filling above the crystalline basement according to INA-CRAS (2004). See text for explanation. (For interpretation of the references to color in this figure legend, the reader is referred to the web version of this article.)
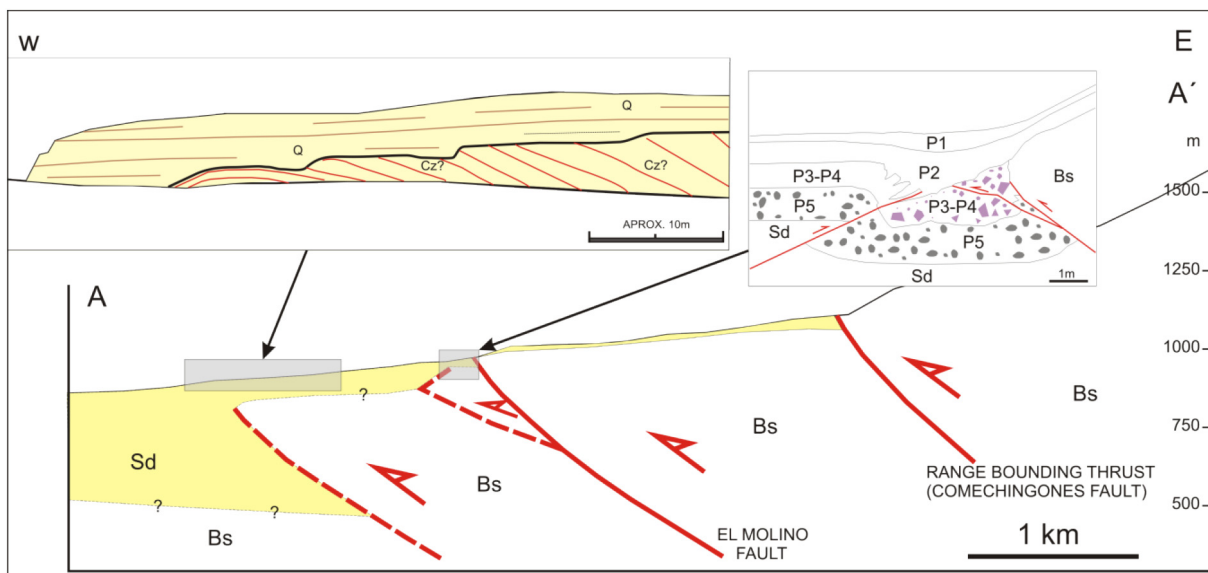
Fig. 3. Interpreted sub-surface structure of the study area. Insets are not to scale. See profile A-A′ location in Fig. 2. Bs, crystalline basement, Sd, sedimentary strata (Paleozoic?-Cenozoic), P, sedimentary packages and faults described in trenches.
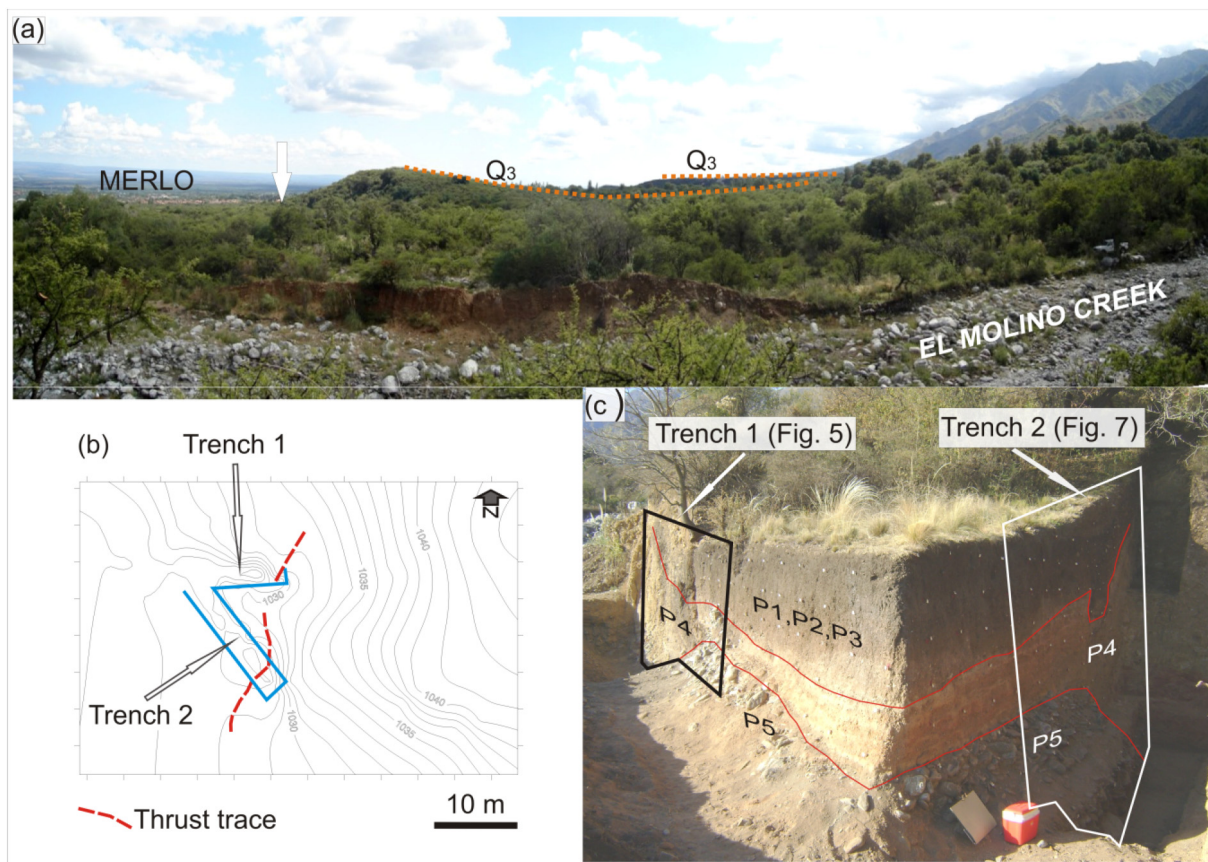
Fig. 4. (a) North-looking view of the Comechingones Range's piedmont foreland as seen from the location of the trenches. The main thrust trace is located at the main slope break (right side of the photo). The El Molino fault trace designated by a white arrow corresponds to the western limit of this piedmont foreland. These hills are capped by alluvial terraces (Q₃) tilted to the east (red dotted lines), whereas younger alluvial surfaces exhibit a gentle slope gently to the west. (b) Topography of the scarp area at the study site. (c) Trenches show the three-dimensional arrangement of main stratigraphic units relative to the deformation zone. See Figs. 5 and 7 for more details. (For interpretation of the references to color in this figure legend, the reader is referred to the web version of this article.)

Several fault sections have been defined along the Comechingones Range piedmont thrusts to discretize domains with similar morpho-tectonic features and landforms assemblages. The fault trace has been inferred for the most part through the interpolation of discontinuous scarps, where no primary morphologies related to faulting have been recognized (Costa et al., 1998, 2014). Thus, the term 'section' here is used in a descriptive way and it should not be regarded as earthquake rupture segments because location and extension of unitary surface rupture lengths remain unknown.

The fault section within our study area, the El Molino fault, is characterized by discontinuous scarps of approximately N-S and NW-SE trends resulting in a staircase array in plan view (Fig. 2). Scarp slopes are composed of a colluvium derived from overlying Quaternary con-glomerates and older rocks. Crystalline basement is very occasionally exposed along creeks beneath older Quaternary alluvial surfaces (Q₃ in Fig. 2), exposing crushed and damaged zones of gneiss, migmatite and sedimentary red beds with variable dips. The piedmont foreland is present along the range front for ~50 km north of 32° 27′S, which this is the southern limit of our study area.

The El Molino fault and related propagating thrusts bound an active area of subsidence to the west. Geophysical exploration and ground-water wells reveal a 400-m-thick succession of Cenozoic (and perhaps older) alluvial strata, where ~200 m is attributed to Quaternary de-posits (INA-CRAS, 2004) (Figs. 2 and 3). The Comechingones Range block has an associated structural relief of ~2200 m at the latitude of our study site (Costa and Morla, 1996), although it is not clear how much of the present structural relief was achieved during the tectonic events linked to the flat-slab subduction. Löbens et al. (2011) have

suggested that the Comechingones Range was part of a Cretaceous rift basin that was tectonically inverted during the Andean orogeny in the Cenozoic. If so, the cumulative Cenozoic uplift must have been larger than indicated by the current structural relief. The Comechingones Range in our study area is composed of Precambrian metamorphic rocks, predominantly light-gray migmatite.

4. Paleoseismic investigations

4.1. Stratigraphy and descriptions of units

Bedrock in the hanging wall corresponds to a shatter zone, where brittle shearing has almost obliterated the original fabric of the mig-matite (Figs. 5, 6 and 7). Cataclastic foliation and layering are evident around a 30-cm-thick zone near the fault surface (Fig. 6a). Pre-Qua-ternary gray/greenish sandstones of unknown age (possibly Late Pa-leozoic) are exposed at the bottom of trench 2 (Fig. 7a and b) and also involved in the deformation of fault F1 (Fig. 5b). Quaternary sediments are mainly exposed at the main thrust footwall (Fig. 5a) and were discriminated as lithofacies units (Fig. 5b) based on their sedimentary fabrics, lithologies, and geometries. A description of the logged units and their numbering scheme is given in Table 1. Logged units were grouped into packages for a synoptic view of the tecto-sedimentary evolution of the deformation zone.

The oldest exposed layers attributed to the Quaternary are com-posed of grayish-brownish gravel (unit 50, trench 1), with a matrix of scarp-derived detritus at its base (unit 51, trench 2) (Figs. 5 and 7).

Units 40, 41 and 42 in the footwall are the result of the hanging-wall
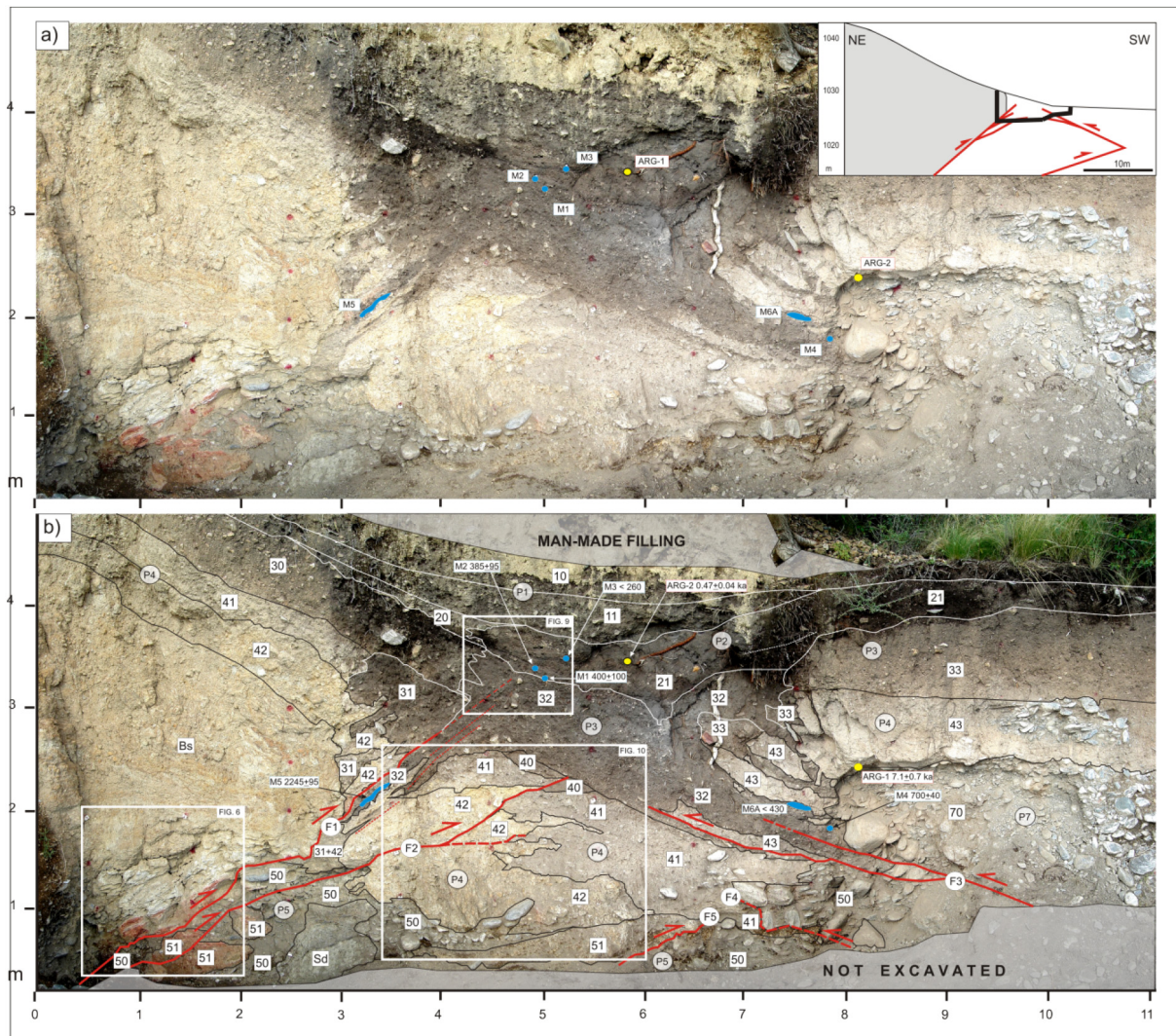
Fig. 5. (a) Photomosaic of the El Molino deformation zone in trench 1, (b) logged lithofacies units and faults (F) (see Table 1 and text for description). Main fault (F1) overrides Precambrian basement (Bs) over Holocene alluvial and colluvial deposits. Faults are indicated by red solid lines and inferred/doubtful structures with red dashed lines. Location of radiocarbon and OSL dating samples are indicated with blue and yellow dots/areas respectively. Interpretation of the deformation zone is sketched in the inset above. All radiocarbon ages expressed in calibrated years BP. (For interpretation of the references to color in this figure legend, the reader is referred to the web version of this article.)

collapse. Some cohesive blocks of gravel at the base of this package abut a basement-derived block. Colluvial wedges are interfingered with wash-slope deposits with sparse subordinated fluvio-aeolian sediments (unit 43). Slope deposit units 41 and 42 on the hanging wall correspond to a regolith of crushed migmatite with lesser amounts of silty-sandy matrix in the bottom unit (Figs. 5a and 7). A significant increase in silty-sandy matrix is apparent in the footwall which has a subtle contact with overlying layers (units 20 and 21).

Units 30 to 33 (Package 3) are mainly colluvial sediments with variable thickness. Different lithofacies with complex lateral transitions are recognized on the basis of clast-matrix ratios and subtle stratification. Subtle east-dipping lineation attributed to the uppermost propagation of fault (F1) is recognized in unit 32, whereas a flat-lying layering characterizes the overlying unit 21 (Fig. 5b).

Units 20 and 21 (Package 2) unconformably overlie older units mostly at fault F1 in the footwall, whereas units 10 and 11 (Package 1) correspond mostly part to the topsoil across both trenches.

4.2. Characteristics of the deformation zone

Excavations at the intersection of the El Molino fault trace with the

El Molino Creek (Fig. 2) (32°21′27.78″S, 64°58′555.64″W) reveal two opposite-dipping thrusts sets that deform Holocene sediments (Figs. 4, 5 and 7). At this site, Costa et al. (1994, 2001), Costa and Vita Finzi (1996) and Murillo (1996) described a natural exposure with metamorphic rocks thrust (here named as fault F1) over scarp-derived colluvium. The original exposure was later enlarged and deepened and a second trench was open into the fault zone (Figs. 4 and 7). The second trench (trench 2) provided a three-dimensional perspective on the deformation and confirmed the structural features previously reported. However, stratigraphic relationships were better exposed in trench 1 for paleoseismic studies.

The east-dipping thrusts correspond to the main deformation zone of the El Molino fault and are interpreted to be the surface expression of the active splay of the Comechingones fault (Fig. 3). Fault F1 places the crystalline Precambrian basement over colluvial and alluvial sediments (Figs. 5 and 7), and has an average strike at trench 1 of 340° with dips varying from 18 to 55° to the east. Crystalline rocks overlie fine-grained sedimentary rocks at trench 2 with a variable NW strike and dip angles < 30°E (Fig. 7c).

Basement rocks are so extensively crushed that it is difficult to distinguish the contact between the bedrock and the colluvial regolith
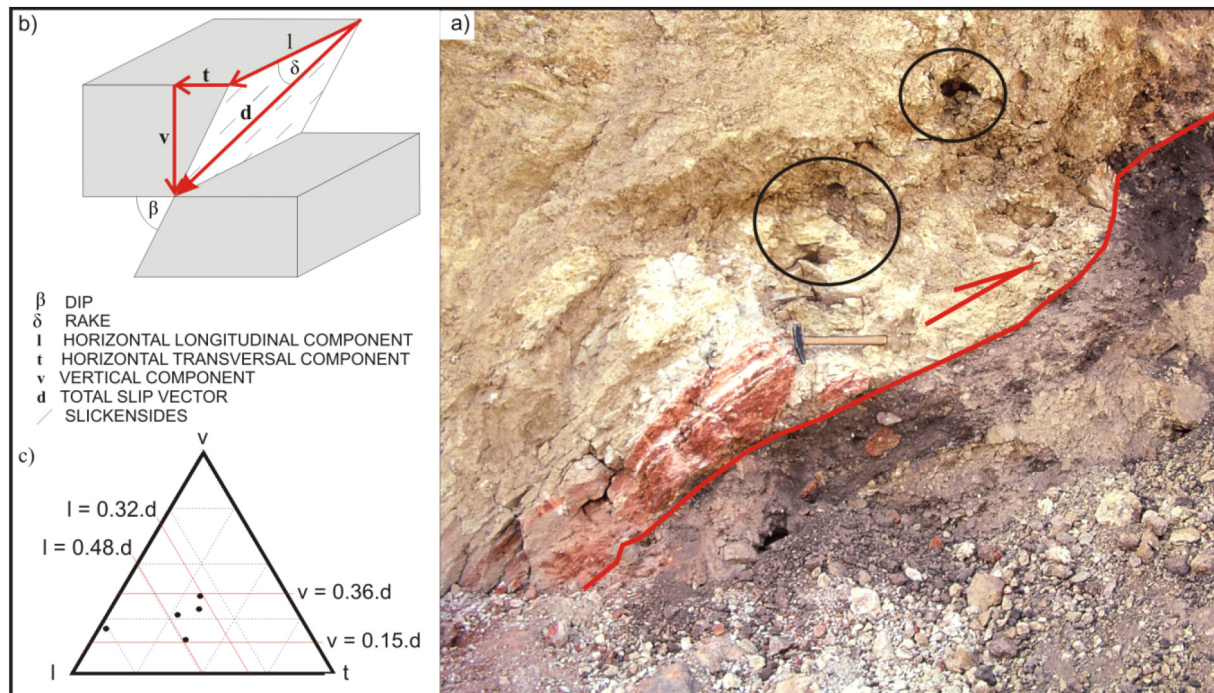
Fig. 6. a) Detail of fault F1 shear zone (40-cm hammer for scale). Despite the intense mechanical modification of the migmatite bedrock, it is possible to recognize control of fault attitude by inherited planar fabric. *In situ* open spaces in basement rocks at the upper part of the photography (circled), suggest this part of the rock massif to have been involved in previous hanging-wall collapse and intense mechanical disaggregation. The dark-colored shear zone in the foot wall contains migmatite clasts and broken gravel clasts. Matrix is composed of gray siltstones. b) Sketch of relations between slip components of fault slip displacement and dip and rake angles. c) Slickensides data measured at fault F1 plotted in a diagram that discriminates the relative participation of each slip component considering a unitary length total slip vector (Costa et al., 1997).

in the overlying sedimentary units (Figs. 5 and 7d). This tectonic contact is characterized by the incorporation of rotated gravel clasts and intercalated material of the footwall unit spaces. This is particularly evident in the lower part of trench 1 (Fig. 6a).

Slickensides have been measured along the main F1 fault plane, indicating that the strike-slip component has a variable importance in the overall displacement of the fault zone. Thus, displacement of layers observed in the trenches should be regarded as the apparent dip slip of the total slip vector. Several fault splays propagating upwards from fault F1 were visible after scraping and logging successive surface exposures of the trench wall (Fig. 5b).

Fault F2 is a secondary east-dipping branch that propagates into the footwall deposits and has a sinuous trace, probably involving minor splays. Although it is difficult to reliably log its trace, it clearly affects units 40, 41 and 42 (Fig. 5b).

The west-dipping fault F3 has dragged unit 50, which is composed of gravels, giving rise to a flexural folding of unit 43. This fault-propagation fold hinge is fragmented by bending-moment fractures and related infilling wedges (Fig. 5). Fault F3 is probably a backthrust driven by underlying west-directed blind structures (Fig. 3). In trench 2, fault F3 corresponds to a bedding-parallel upthrust in the sedimentary bedrock, which propagates concave downwards through the loose fabric of units 50 and 51 (Fig. 7a and b).

Fault F4 trace was interpreted as a backthrust because unit 50 is above unit 41 due to a fault slippage affecting unconsolidated sediments with rotated gravels clasts and an interpenetrated fabric. (Fig. 5). This fault has not been recognized in trench 2. Fault F5 is interpreted as a splay related to main fault F1, which overrides units 50–51 gravels over scarp derived deposits (unit 60) in trench 1.

Other east-dipping blind or barely emergent thrusts are interpreted to underlie these exposures. This view is supported by gently folded Quaternary gravels to the west of the trenches and a remarkable increase in thickness (~400 m thick) of Cenozoic (and older?) sediments

beneath Merlo village, as imaged by geophysical data and boreholes (INA-CRAS, 2004) (Figs. 2 and 3).

4.3. Sediment ages

Charcoal and organic-rich sediments appropriate for radiocarbon dating are preserved in packages 2 and 3 (Table 2). AMS radiocarbon dating was undertaken on detrital charcoal (samples M1 to M4) and bulk sediments samples containing ~4% organic carbon (samples M5 and M6; see Fig. 5b and Table 2). Sample M5 yielded older ages than previously determined by Costa and Vita Finzi (1996) along the same fault sector (conventional radiocarbon dating ages of 1170–800 and 1300–1150 cal yr BP). Several palynomorph specimens were reported in bulk samples M5 and M6 and are interpreted as the original organic content of these sediments, rather than lixiviated carbon separated from younger overlying layers (Silvia Grill *written communication*).

The sediment samples for OSL dating (ARG-1 and ARG-2; Fig. 5b and Table 3) were collected by driving light-tight plastic tubes, 5-cm-diameter and ~30-cm-long, into freshly exposed sections. Approximately 200 g of sediment was collected from the sampled sediment and where the sediment was heterogeneous or where the sampled unit was < 30 cm thick we collected additional sediments from above and below the sample. These samples were used for determining dose rates using neutron activation analysis (NAA) and measured *in situ* as well. Very young samples (such as ARG-2) are very sensitive to partial bleaching problems. Since slight partial bleaching can have a higher percentage impact on younger than older samples, ARG-2 should be considered a maximum age. Nevertheless, the OSL age for ARG-2 (0.47 ± 0.04 ka) is similar to the radiocarbon ages for samples M1, M2, and M3.

Sample ARG-1 (7.1 ± 0.7 ka) was obtained at the boundary between units 43 and 70, limiting the younger age of the latter gravely unit, used as a geometric marker for estimating deformation at this site.
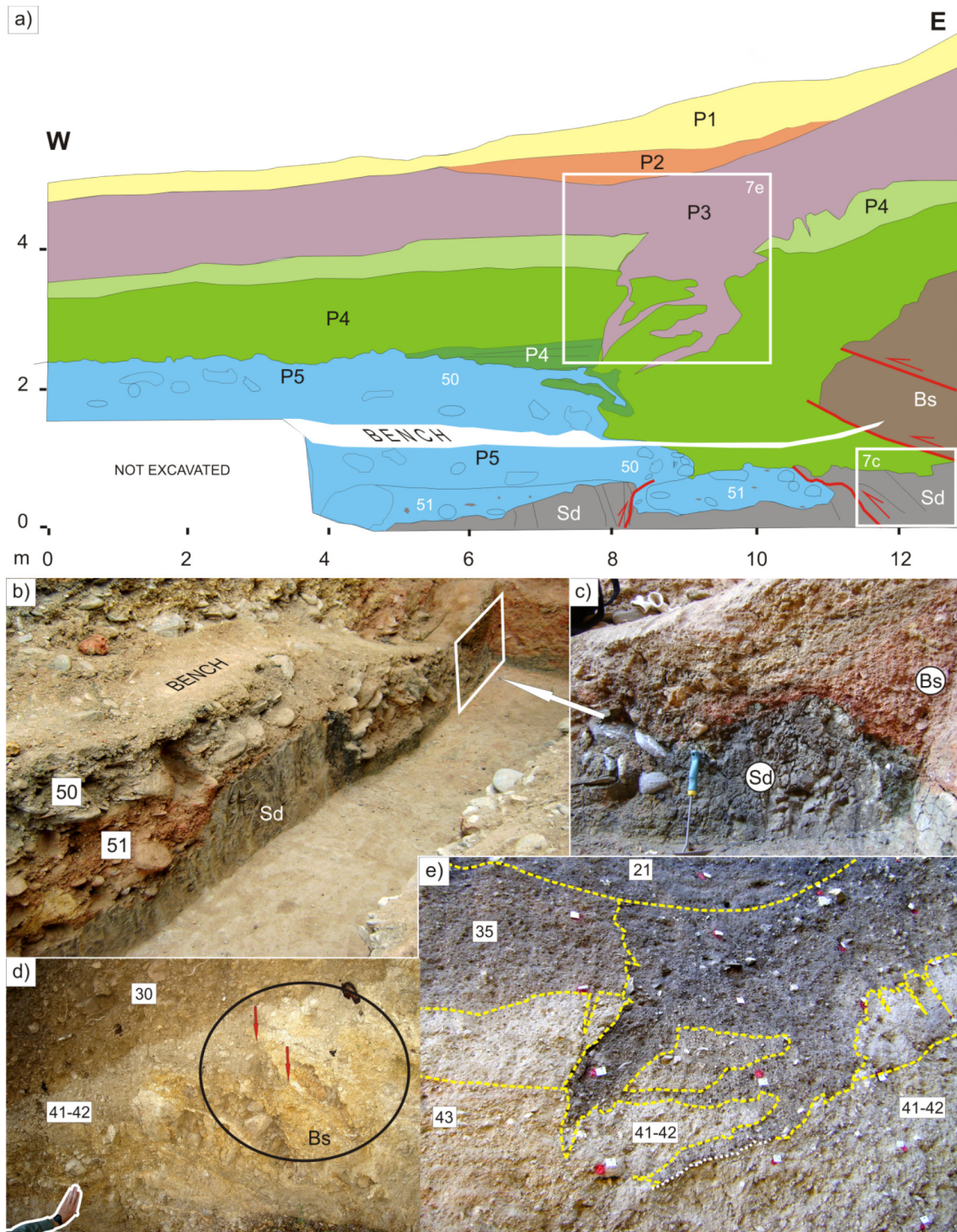
Fig. 7. a) Schematic log of deformation zone in trench 2 (north wall) with the same identification of packages and units as for trench 1. Sd, gray-greenish siltstones; Bs, crystalline basement. b) South wall of trench 2 (flipped), exposing the erosion surface separating sub-vertical strata (Sd) from the gravels of unit 51 (reddish matrix derived from colluvial detritus), overlaid by gravels of unit 50. c) Detail of the tectonic contact of the shattered reddish basement rocks (Bs) thrusting sedimentary layers (Sd). The scraper is 35 cm. d) East-dipping subparallel thrust rupturing basement rocks and units 41 and 42. Photograph was taken upslope of the trench log represented in panel a. e) Detail of the co-axial depression between the opposite-verging thrusts, where same units as logged in trench 1 can be recognized. See white quadrangle in panel a for location. Trench log (a) and photo detail (e) correspond to different exposures of the trench wall. (For interpretation of the references to color in this figure legend, the reader is referred to the web version of this article.)

Table 1
Description of the lithofacies units indicated in Fig. 5b.

Unit	Composition
Package 1	
10	Black-brownish coarse colluvium including the top soil. At the scarp slope, angular clasts of basement rocks (≤ 20 cm-long axis) with matrix support are dominant with maximum thickness up to 50 cm. Thickness at the scarp base is < 20 cm with less participation of basement clasts and a sandy-silty matrix, typical of wash-slope deposits. The A horizon of the top soil is better defined here.
11	Brownish coarse colluvium mostly developed at the scarp base, with similar composition than unit 10, but less organic matter. It has a lens-shaped geometry with a flat top. Contact with Unit 10 is transitional whereas it exhibits a clear and net boundary with Sequence 2. Sediments of this unit encompass the transition zone between debris slope and wash slope deposits.
Package 2	
20	Dark colluvial deposit with silty-sandy matrix, poorly layered and strongly bioturbated by roots. It corresponds to a localized infill at the scarp base. Organic-rich fine-grained sediments are dominant. Palynological content (mainly *Bidens* sp., *Ambrosia* sp. *Gonfrena* sp.), and abundant phytoclasts (S. Grill, written communication) are consistent with a poorly drained and occasionally ponded sector (S. Grill, written communication).
21	Grayish-colored unit with a variable participation of clasts and matrix and scattered angular clasts. Occasionally with flat-lying thin layers of sand and gravels. Shows dominance of organic-rich silty sediments where charcoal for ^{14}C dating was collected (Samples M1, M2, and M3). Sample M1 lies in the interpreted contact with the underlying Sequence 3.
Package 3	
30	Coarse brownish colluvium with angular clasts of weathered basement rocks (≤ 5 cm-long axis). Most clasts are coated with carbonates. Silty matrix increases from east to west.
31	Unsorted proximal coarse deposit. It shows a mixed participation of collapsed fragments derived from the hanging-wall with fine-grained sediments deposited at the footwall, which results in darker colors than unit 30. Along the contact with the hanging-wall these dark sediments alternate with light-colored of gravity-driven fragments of migmatites, suggesting that deposition of these colluvial deposits with sandy-silty matrix was coeval with the hanging-wall collapse
32	Silty dark-colored deposit with scattered angular basement clasts. This unit could be subdivided into several sub-units depending on the basement clasts participation and shear fabric imposition. The bottom part of this unit is stacked against the main fault zone, where sample M5 was obtained. These dark sediments fill the depression bounded by faults F1 and F2. Sediments with a mixed participation of this unit and unit 43 constitute the filling of the extensional cracks of the fold related to the propagation of fault F3. Samples M4 and M6 obtained within this highly transposed zone, yielded ages of 700 + 40 cal yr BP and < 430 cal yr BP respectively (Fig. 5).
33	Similar composition than unit 32, but with more participation of sand and gravel with a rough layering to the west of fault F3. This unit corresponds to wash slope deposits, developed mainly at the back limb of the fault-propagation fold related to fault F3.
Package 4	
40	Coarse brownish deposits of massive fabric. Dominates a silty composition with subordinated angular sand-size angular clasts and occasional angular clasts (≤ 5 cm). It has a participation of organic matter in its fabric (< 1.5%). Bottom and top contacts are erosive and disrupted by fault F2.
41	Light-colored deposit composed of basement-derived angular granules with a silty matrix. It can be distinguished from unit 40 because there is more participation of silty sediments of aeolian provenance. At fault F1 hanging-wall, it is constituted by slope deposits with > 90% of participation of crushed basement rocks and minor participation of silt and sand. At the foot-wall, this unit exhibits a massive fabric and it is interpreted to interfingered with unit 42 in a complex colluvial wedges framework. It seems to be dominated by wash slope deposits.
42	Although with very similar composition, above the hanging-wall this unit is characterized by slope deposits made up almost exclusively of the loose fragments of the basement top. It is very difficult to distinguish the boundary between this regolith and the *in situ* crushed rocks. This unit has same lithological composition and aspect than the crystalline basement. Hill-creep processes enabling detachment from the *in situ* rocks are suspected to be present in this light-colored tabular layer. At the foot-wall they correspond to gravity-driven deposits from the collapsed hanging-wall, both the *in situ* basement and overlying slope deposits. It is considered as a stacked colluvial wedge, highlighted by light colors and a notable dominance of basement blocks with very different fabric orientations. Fluvial gravels are present at the base of this unit. These materials are usually reactive to HCl. At least two stone lines can be distinguished at the interaction zone with unit 41.
43	Massive light-gray deposit with scattered angular granules in a silty-sandy matrix. It is reactive to the HCl and lenses of fluvial gravels are present. This unit has been buckled by fault F3 propagation and as a consequence, bending-moment fractures have been developed in the hinge area. It is conceived to correspond to lithofacies more distal to the scarp correlative with the other units of this sequence, where wash slope deposits prevail in interaction with fluvial intercalations and aeolian input. These lateral relations cannot be clearly outlined due to fault transposition.
Package 5	
50	Gray gravels of fluvial origin of different sizes (average 10 cm, largest 90 cm). Matrix is composed of loose sand and granules sometimes coated with carbonates. In the hinge zone related to fault F3, the fabric completely loose with open spaces. A mica-rich sandy matrix dominates near the fault scarp with layers of unconsolidated gray sand, disrupted by faults F1 and F2.
51	This unit of reddish-orange tones is composed of fragments of highly altered migmatites restricted to the fault zone of f1 and f2. It exhibits a subtle flat-lying planar fabric due to intercalation with subordinated fluvial gravels (better exposed in the trench 2). They could represent either basement slices dragged by fault slip or hanging-wall collapsed blocks. Hand-lens observation allows recognizing rounded grains of quartz, suggesting a mixed colluvial/alluvial origin.
Sedimentary bedrock	
Sd	Greenish to grayish massive pelites with subordinated light-colored sandstones. Exhibit in trench 2 an almost vertical attitude with evident signals of shearing or cataclastic-driven planarity. This lithology is barely exposed dragged by fault F1
Crystalline basement	
Bs	Highly sheared migmatites of yellowish-grayish (occasionally reddish) colors. Primary mica and feldspar are almost completely altered by friction. Shear phenomena and main fault surface follow metamorphic fabric.

There was no paleosol development at the boundary between these two layers, so it is assumed that the time gap between deposition of these units was not significant.

5. Discussion

5.1. Tectonic-sedimentary evolution

Stratigraphic units preserved in the footwall of fault F1 show that coarse gravel deposition was the dominant process for emplacement of the oldest layers above the foot wall bedrock (unit 50, ~7 ka; Figs. 5b and 7b). The main fault scarp was then providing limited scarp-derived detritus, eventually mixed with alluvial gravels (unit 51, Fig. 7a and b). Subsequent deformation driven by slippage mostly along fault F1 resulted in successive scarp growth and the dominance of colluvial slope deposits in the footwall. These gravity-driven deposits (units 40, 41 and 42) thin away from the main fault F1, where slope-wash deposits dominate (unit 43) (Figs. 5b and 8). The present arrangement of units

Table 2

Radiocarbon (^{14}C) dates of samples analyzed at Beta Analitic Inc. Calibrated ages obtained using INTCAL13 Radiocarbon Age Calibration (Reimer et al., 2013). See text for other details.

Sample ID	Lab. ID	Material	Measured Radiocarbon Age (yr BP)	13C/12C Ratio	Conventional Radiocarbon Age (cal yr BP)	14C age cal yr BP (2σ)	Mean age cal yr BP (2σ)
M1	Beta - 263681	charcoal	340 +/− 40	− 24.2 ‰	350 +/− 40	495 − 311	403 + 92
M2	Beta - 263682	charcoal	300 +/− 40	2 25.0 ‰	300 +/− 40	474 − 288	381 + 93
M3	Beta - 263683	charcoal	102.3 +/− 0.5	− 9.7 ‰	60 +/− 40	266 − 22	144 ± 122
M4	Beta - 263687	charcoal	660 +/− 40	− 18.1 ‰	770 +/− 40	765 − 661	713 ± 52
M5	Beta - 263685	organic-rich sediment	2110 +/− 40	− 16.9 ‰	2240 +/− 40	2342 − 2153	2247 ± 95
M6A	Beta - 263686	organic-rich sediment	270 +/− 40	− 25.4 ‰	260 +/− 40	458 − 149	303 ± 155

41 and 42 near faults F1 and F2 is interpreted as a fragmented warping of this colluvium consistent with thrust fault evolution.

Propagation of antithetic thrust faults related to the west-dipping thrust set caused folding of units 50 and 51 and flexure and fragmentation of unit 43, leading to the formation of hinge-related fractures that filled in with overlying sediments of unit 32. Unit 40 indicates the beginning of scarp-related deposits with the dominance of matrix-supported rather than clast-supported deposits. This change in the depositional environment at the scarp base may be related to a decrease in the slope angle due to the propagation of west-dipping thrusts. The activity of this thrust set could have resulted in a gentle counter-slope above the frontal limb of the fold. This is less evident in trench 2 due to thicker slope deposits. Nevertheless, the geometry of units 20 and 21 (package 2) at both trenches highlights a co-axial depression at the scarp base (Figs. 5b and 7e). Also, lesser amounts of materials derived from the hanging wall might suggest a temporary quiescence of fault F1 at this time.

West-dipping faults probably did not rupture to the surface. The local marsh environment exposed at both trenches was filled with organic-rich fine colluvium and representative palynomorphs from local ponding in semi-arid environments (mainly *Bidens* sp., *Ambrosia* sp., *Gonfrena* sp., and abundant phytoclasts; Silvia Grill, *written communication*). Units 10 and 11 correspond to depositional conditions prevailing today.

5.2. Interpretation of surface deformation events

Although evidence for surface deformation is clear in the study site, it is challenging to discern the number of deformation events involved and to date them individually. On one hand, it is difficult to decouple surface deformation evidence from similar lithofacies resulting from different factors (climatic processes, ground shaking driven by other sources or by blind faults). Interpreting whether slip events have occurred along more than one fault simultaneously or if observed displacements have resulted from single or multiple events is not possible. However, evidence for a minimum of three and a maximum of nine deformation events is discussed below. Deformation events termed "possible" are rooted in evidence judged to be ambiguous or somewhat controversial. The interpreted events listed below are from young to old and shown in terms of horizons in Fig. 8.

Possible event 1. Package 2 is characterized by fine-grained sediments at the scarp toe, whereas package 1 overlies this part of the scarp with dominantly angular clasts, larger in size (Table 1) and tends to thicken at the scarp base. This change might be due to a climatic signal or an earthquake-induced shaking related to underlying faults.

Possible event 2. The counter-slope contact between packages 2 and 3 above the west-dipping thrusts (Fig. 5a) may be considered an anomalous slope angle for the deposition of currently east-dipping fine-grained sediments (unit 21), with layering parallel to the top of package 3. We could not determine whether this local depression corresponds to inherited topography or if it was the result of propagation of west-dipping thrusts after the deposition of package 2.

Event 3. Evidence for this event includes several subtle subparallel lineations in the massive deposits of unit 32 (package 3), which are aligned with the upward projection of fault F1 (Fig. 9). An OSL age of 0.5 ± 0.1 ka (sample ARG-2) obtained in unit 21 and a radiocarbon age of 403 ± 92 cal yr BP (sample M1) for the contact between packages 2 and 3 brackets the minimum age for this event or events.

Event 4. Angular relationships between units 32 and 43 above the fault F3 suggest the occurrence of at least one deformation event

Table 3

Samples details, nuclide concentrations, dose rates and ages for OSL samples.

Sample	Location (°S/ °W)	Altitude (m asl)	Depth (cm)	Lithology	Sediment type	Particle size (μm)	Water content (%)	Total dose-rate (Gy/ka)[a,b,c]	Number of aliquots[d]	Mean equivalent dose[e] (Gy)	OSL age[f] (ka)
ARG-1	32.357/64.982	1005	210	Poorly sorted sands	Fluvial	90–125	3	3.44 ± 0.34	**16** (39)	24.6 ± 0.8	7.1 ± 0.7
ARG-2	32.357/64.982	1006	105	Pebbly sandy silts	Fluvial	180–250	2	3.73 ± 0.21	**21** (46)	1.8 ± 0.1	0.47 ± 0.04

[a] Estimated fractional present-day water content for the whole sediment is taken as 10 ± 5% for dose rate calculation.

[b] Estimated contribution to dose-rate from cosmic rays calculated according to Prescott and Hutton (1994). Uncertainty has taken as ± 10%.

[c] Total dose-rate from beta, gamma, and cosmic components. Beta attenuation factors for U, Th and K compositions incorporating grain size factors from Mejdahl (1979). Beta attenuation factor for Rb is taken as 0.75 (*cf.* Adamiec and Aitken, 1998). Factors utilized to convert elemental concentrations to beta and gamma dose-rates from Adamiec and Aitken (1998) and beta and gamma components attenuated for moisture content. The mean and 2 sigma error is used where multiple dose rates were determined for a simple.

[d] Number of replicated equivalent dose (DE) estimates used to calculate mean DE shown in bold. These are based on recuperation and reproducibility errors of < 10%. The number in the parenthesis is the total measurements made including failed runs with unusable data.

[e] Weighted average equivalent dose (DE) determined from replicated single-aliquot regenerative-dose (SAR; Murray and Wintle, 2000) runs. The uncertainty also includes an error from beta source estimated of ± 5%.

[f] Uncertainty incorporate all random and systematic errors, including dose rates errors and weighted average uncertainty for the DE.
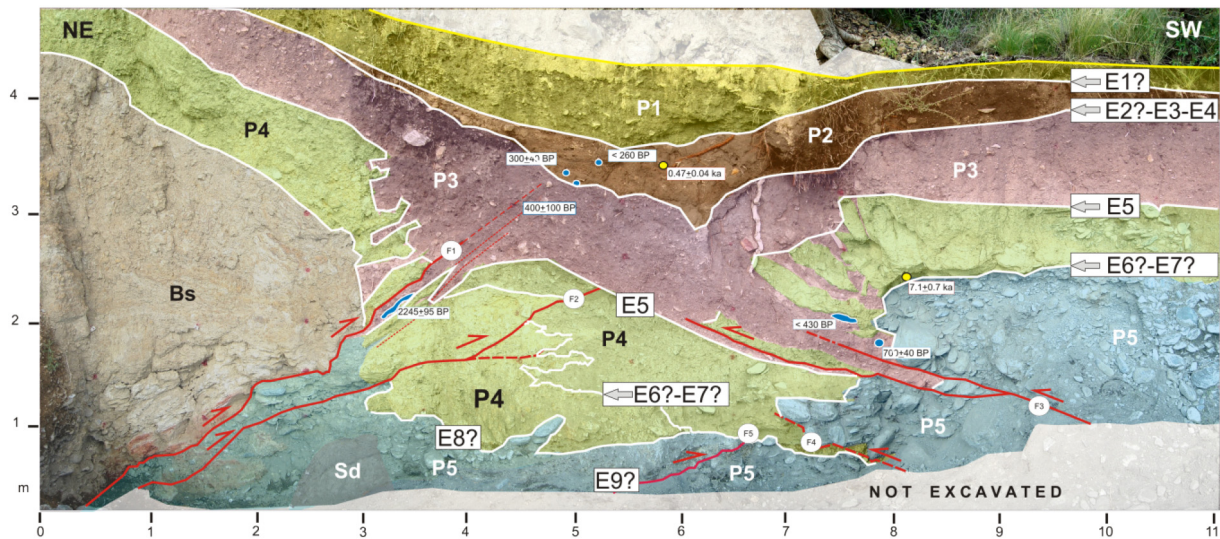
Fig. 8. Sedimentary packages (P) disposition at the El Molino deformation zone in trench 1, where many faults (F) are exposed (see Table 1 and text for description). Main fault (F1) overrides Precambrian basement (Bs) over Holocene alluvial and colluvial deposits. Faults are indicated by red solid lines and inferred/doubtful structures with red dashed lines. Location of radiocarbon and OSL dating samples are indicated with blue and yellow dots/areas respectively. Horizons of interpreted deformation events (E/E?) are indicated by white solid lines. See text for explanation. (For interpretation of the references to color in this figure legend, the reader is referred to the web version of this article.)
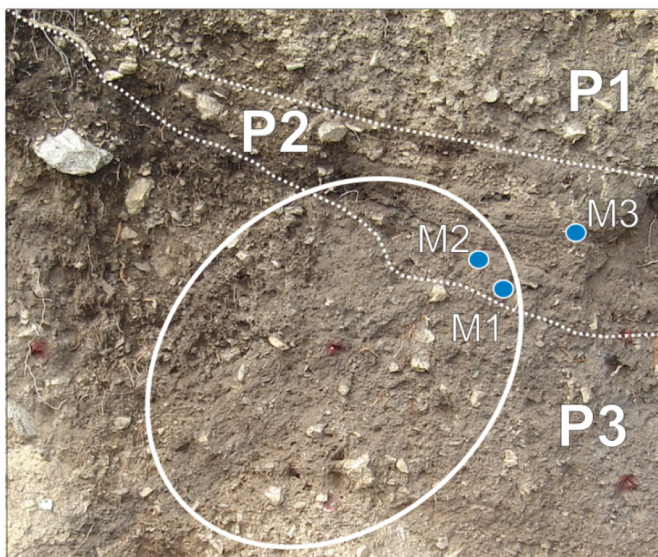
Fig. 9. Detail of composition and fabric arrangement of packages (P) 1, 2 and 3 (see location in Fig. 5b). White ellipse spotlight differences between the sub-horizontal layering characterizing package 2 and the massive and coarse fabric of package 3. Sub-parallel east-dipping lineations more obvious at the lower left of the photo truncated at the top of package 3 are considered to represent the propagation fabric of fault F1 in poorly consolidated sediments.

(Fig. 5b). This induced surface flexure and fragmentation of unit 43 after the deposition of package 3. Fault F3 slip and related bending cracks at the fold hinge, filled with unit 32 sediments, support this statement. The massive fabric of the filling material has prevented us from discerning whether more than one infill episode occurred. A maximum radiocarbon age of 303 ± 155 cal yr BP (sample M6A) was obtained for sediment within the filling wedges (Fig. 5 and Tables 1 and 2). However, this age was considered suspiciously young in comparison with the results of nearby samples and was therefore not used in our interpretation. It is not possible to elucidate whether this deformation occurred simultaneously with fault F1 during event 3.

Event 5. Unit 40 corresponds to a colluvial wedge, probably thickened by subsequent thrusting. Unit 41 is entirely composed of hanging-
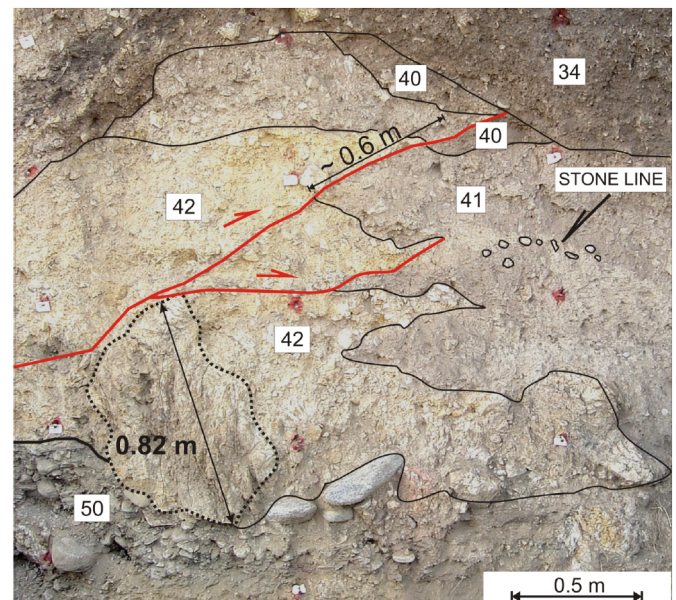
Fig. 10. Detail of fault F2 affecting package 4 units. Yellowish colors of a transposed colluvial wedge (unit 42) contrast with grayish-brownish tones of colluvial and slope-wash deposits of unit 41. Dotted line contours a migmatite block collapsed from fault F1 hanging-wall. Thin solid lines enhance the metamorphic planar fabric, indicating that this block fell as a single piece. See Fig. 5b for location. (For interpretation of the references to color in this figure legend, the reader is referred to the web version of this article.)

wall debris, with internal open spaces and without allochthonous material in its matrix. This unit is interpreted as having been derived from coseismic hanging wall (free face) collapse and exhibits a massive, coarse and loose fabric. Slip along fault F2 has clearly disrupted colluvial-wedge deposits (units 40, 41 and 42) without affecting package 3 (Fig. 10). Contact between units 32 and 40 suggests an eroded top of unit 40 rather than a larger number of events affecting unit 41.

Possible event 6. Unit 41 is interfingered with the wash-slope deposits of unit 42 and is dominated by colluvial or wash-slope deposits at the scarp base. The sharp contact of unit 41 overlying unit 42, could be

interpreted also as a flat thrust splay (Fig. 10). If this contact were erosive, a new breakthrough of the colluvial deposits may have been triggered by main scarp reactivation driven by the activity of fault F1 or by a climatic event. A stone line also highlights this situation (Fig. 10).

Possible event 7. Another colluvial wedge protruding into the wash slope deposits of unit 42 below fault F2 flat splay can also be interpreted as indirect evidence of scarp reactivation due to coseismic slip of fault F1 and/or associated structures (E7? in Fig. 8). These kinds of features can be attributed to event horizons as defined by Nelson (1992) and McCalpin and Carver (2009), but they could also result from debris deposition induced by climatic events or ground shaking without rupture related to the study faults.

Possible event 8. Colluvial wedge deposits of package 4 overlie alluvial gravels, implying a sudden change in the depositional conditions at the footwall of fault F1. This change is possibly linked to a significant (coseismic?) collapse of the thrust hanging wall in trench 1 (Figs. 5b and 8). No paleosol development or other internal layering was distinguished within this massive unit, suggesting a single major hanging-wall collapse or several episodes of deposition closely spaced in time.

Possible event 9. Another event might be represented by the net contact between predominantly colluvial deposits of unit 51 overlying the fluvial gravels of unit 50 (Figs. 5b and 8). Nevertheless, the erosive or tectonic nature of this contact could not be properly elucidated.

Assuming that unit 50 correlates at both walls of fault F3, as observed in the trench 2 (Fig. 7), the deformation events interpreted above should have taken place during the past ~7 ka.

5.3. Coseismic slip and magnitude estimation

The lack of suitable geometric markers in both trenches makes it difficult to constrain single event displacements. An attempt to assess a possible slip per event can consider fault F2 overthrust of unit 42 (Fig. 8), which accounts for a minimum dip slip of ~0.6 m if related to a single displacement. Similar displacements have been noted in trench 2 (Fig. 7d).

A few slickensides surveyed on fault F1 surface indicate that the relative participation of the horizontal longitudinal slip may range from 32 to 48% of the total slip vector (Fig. 6b and c). This estimation is derived from dip and rake angles plotted on a ternary graph (Costa et al., 1997). Thus, a dip-slip of 0.6 m also suggests single events displacements of ~1 m. No reliable kinematic indicators have been found to determine the nature of the strike-slip motion.

A hanging-wall block lying inside the colluvial wedge (unit 42) with a long axis of 0.82 m in trench 1 wall (Fig. 10) might have collapsed from a sudden coseismic scarp rise. Although the hanging wall may also have fallen from the upward slope without relation with a surface rupture, so caution is needed when considering this observation as possible evidence of coseismic slip. If linked to fault slippage, this collapsed block also points to vertical slips of meter/sub-meter scale.

Common approaches for estimating the magnitude of prehistoric earthquakes rely on empirical relationships relating earthquake size with surface rupture length, rupture area or coseismic displacement (Wells and Coppersmith, 1994; Stirling et al., 2013, among others). The geomorphic imprint of the El Molino fault trace corresponds to discontinuous, multi-event or composite scarps (Figs. 1 and 2), without preservation of primary fault-related morphologies and thus is not suitable for recognition of individual rupture lengths. This primary shortcoming, plus other uncertainties outlined by researchers such as Stirling et al. (2002) and McCalpin (2009), show that the rupture length method is not appropriate for studies such as ours.

The total slip vector related to at least one rupture event undergone by fault F2 and perhaps fault F1 could be ~1 m, rendering the coseismic displacement approach more promising for paleoearthquake magnitude estimations. Available worldwide scaling laws for reverse faults including oblique slip at intraplate settings or slow faults (see Stirling et al., 2013 for a review) with a maximum displacement of 1 m are associated with a magnitude of 6.6 (Wells and Coppersmith, 1994), and magnitude 7.0 for average displacement estimation (Biasi and Weldon II, 2006).

5.4. Time since the last movement

Trench 1 log (Figs. 5b, 8 and 9) shows different sedimentary fabric arrangements between packages 2 and 3. Parallel subtle lineations on unit 32 (package 3) cannot be ascribed to primary sedimentary structures but are tectonic lineations related to fault F1's propagation. Primary layering disruption controlled by shear is more obvious at the bottom part of this unit, highlighted by intercalations of organic-rich sediments and basement rocks. Detailed observations favor a link with these linear features and propagating cracks or microfractures with fault F1 propagation. In contrast, unit 20 (package 2) exhibits flat layering composed by intercalations of gravely sand and fine-grained organic-rich sediments, with a typical geometry associated with infilling deposits (Fig. 9). Colluvium supply was almost negligible. We interpret this unit boundary to separate the youngest deformed layers (unit 32) from those not affected by the east-dipping thrusts propagation (unit 20). Samples M1 (403 ± 92 cal yr BP) and M2 (381 ± 93 cal yr BP) of charcoal-bearing strata lie at the boundary of these units, but we are more confident to include these samples within the unit 20 domain (Fig. 7). An OSL age of 0.5 ± 0.1 ka (ARG-2) was obtained in adjacent unit 21. Events E1 and E2 must have occurred before the first Spanish settlers arrived in the region during the first half of the 18th Century, otherwise, we would have historical accounts of these earthquakes. Accordingly, the most recent surface rupture event is considered to have occurred before 0.3–0.5 ka.

Bulk samples of unit 32 displaced by fault F1 thrusting, yielded radiocarbon ages of 2245 ± 95 cal yr BP (sample M5), bracketing the lower boundary for the last event/s affecting the study sequence. Samples M4 (700 ± 40 cal yr BP) and M6A (< 430 cal yr BP) have probably yielded to suspiciously young ages for unit 32 (Fig. 5b) implying the last rupture to have taken place during the last 0.3–0.5 ka. Thus, considering the available data, the best estimate lower time boundary for the last event/s may varies approximately from 2245 ± 95 and 700 ± 40 cal yr BP.

5.5. Threshold earthquake for producing primary surface rupture

Surface faulting such as documented here must be linked to crustal earthquakes of magnitude ≥6.6 according to the estimated coseismic slips. This magnitude gives a 70% probability of surface rupture considering historical data on reverse faults (Lettis et al., 1997). Historic crustal earthquakes in the Sierras Pampeanas (M ≤ 6.5, IMM ≤ VIII) have left no evidence of primary surface deformation (INPRES, 1977). This suggests that the evidence of surface deformation at our study site accounts for larger earthquakes than those recorded in the seismic catalog.

The M_s 6.0 Sampacho earthquake of 1934 (Fig. 1a) generated widespread liquefaction (Mingorance, 1991; Sagripanti and Villalba, 2011), although the occurrence of primary ruptures was not observed or demonstrated. Ruptures associated with the 1977 M_w 7.4 Caucete earthquake (19 km depth) (Fig. 1a) occurred at the westernmost Pampean range and resulted in sub-metric discontinuous scarps with a graben-like array, without geometric and kinematic connection with the main source. This event, located near the front of the colliding zone with the Andean orogenic front, was due to a blind compressive rupture (Kadinsky-Cade et al., 1985; Langer and Hartzell, 1996; Alvarado and Beck, 2006). Thus, these sub-metric vertical coseismic ruptures at the surface should be ascribed to secondary distributed deformation.

Consequently, it is possible that coseismic displacement at the study site could have been larger than we suggest, meaning that the threshold magnitude for triggering primary surface deformation could have had a magnitude of ≥7. Otherwise, the applied scaling laws may

underestimate the size of paleoearthquakes in the Pampean Ranges region (Costa, 2005).

Surface ruptures of reverse faults are challenging to link with diagnostic morphologies and with unitary rupture lengths in most morphotectonic settings (McCalpin, 2009). In compressive intraplate areas, surface rupture may be expressed by short and discontinuous scarps, but may also be obscured by thick modern alluvium (Lettis et al., 1997; McCalpin and Carver, 2009; Clark et al., 2014). Not surprisingly, application of the rupture length/rupture area method through several equations assuming a rupture length of 5 km and a rupture area of 75 km^2, led to estimate magnitudes of prehistoric earthquakes of M_w 6.3–6.6 (Wells and Coppersmith, 1994; Berryman and Villamor, 2004) and M_w 5.6–5.9 (Anderson et al., 1996; Wesnousky, 2008; Leonard, 2010). This magnitude range is represented in the seismic catalog (INPRES, 1977) without evidence for primary ruptures and thus falls below the threshold magnitude expected for surface faulting. Empirical regressions based on rupture length and rupture area criteria developed for other regions likely underestimate the threshold earthquake magnitude for producing primary surface deformation in the Pampean Ranges area.

5.6. Shortening rate

We cannot develop a reliable estimation of deformation rate due to the lack of continuous strain markers with known ages on both sides of the main fault (F1). Rather, our efforts have been focused on assessing possible minimum and maximum values of shortening supported as by the available exposures. Accordingly, a couple of alternatives were selected to limit what we understand could be the minimum and maximum slippage for the past ~7 ka. Potential variables affecting the

Table 4

Shortening estimations resulting from line restoration of the top (1) and the base (2) of package 5 and age values used for shortening rates assessment. Maximum rate resulted from considering maximum shortening (1) and minimum age (3) obtained for the geometric marker, whereas the minimum rate was derived from the ratio minimum shortening (2) vs. maximum age (4).

Deformed line length –top of unit 50, trench 1-	11.6 m
Restored line length -green marker trench 1-	17.8 m
Deformed line length –top of foot wall bedrock, trench 2-	8.0 m
Restored line length –top of footwall bedrock, trench 2-	12.1 m
Maximum shortening –green marker trench 1- (1)	6,2 m
Minimum shortening (2)	4.1 m
Minimum age sample ARG-1 (3)	6.4 ka
Maximum age sample ARG-1(4)	7.8 ka
Maximum shortening rate (1/3)	0.97 mm/a
Minimum shortening rate (2/4)	0.53 mm/a
Mean shortening rate	0.7 ± 0.2 mm/a

measurement of present deformation through line wire restoration of unit 50, such as changes in density/volume and internal shear was not taken into account.

To approach a possible maximum value for shortening, we use the top of unit 50 in trench 1 as a strain marker, assuming to be the same layer displaced by faults F2 and F5 (green line in Fig. 11a). Displacement along fault F1 (trench 1) can place limits on the shortening undergone by this structure and the top of unit 50. Unit 42 pendants on the hanging wall (point 1 in Fig. 11a) represent under this assumption the total displacement by fault F1 after unit 50 deposition (point 1′ in Fig. 11a). This yields 6.2 m of total shortening.

Another approach is to use the erosive surface at the base of unit 51 exposed in trench 2, as a different deformation marker (Fig. 7a and b).
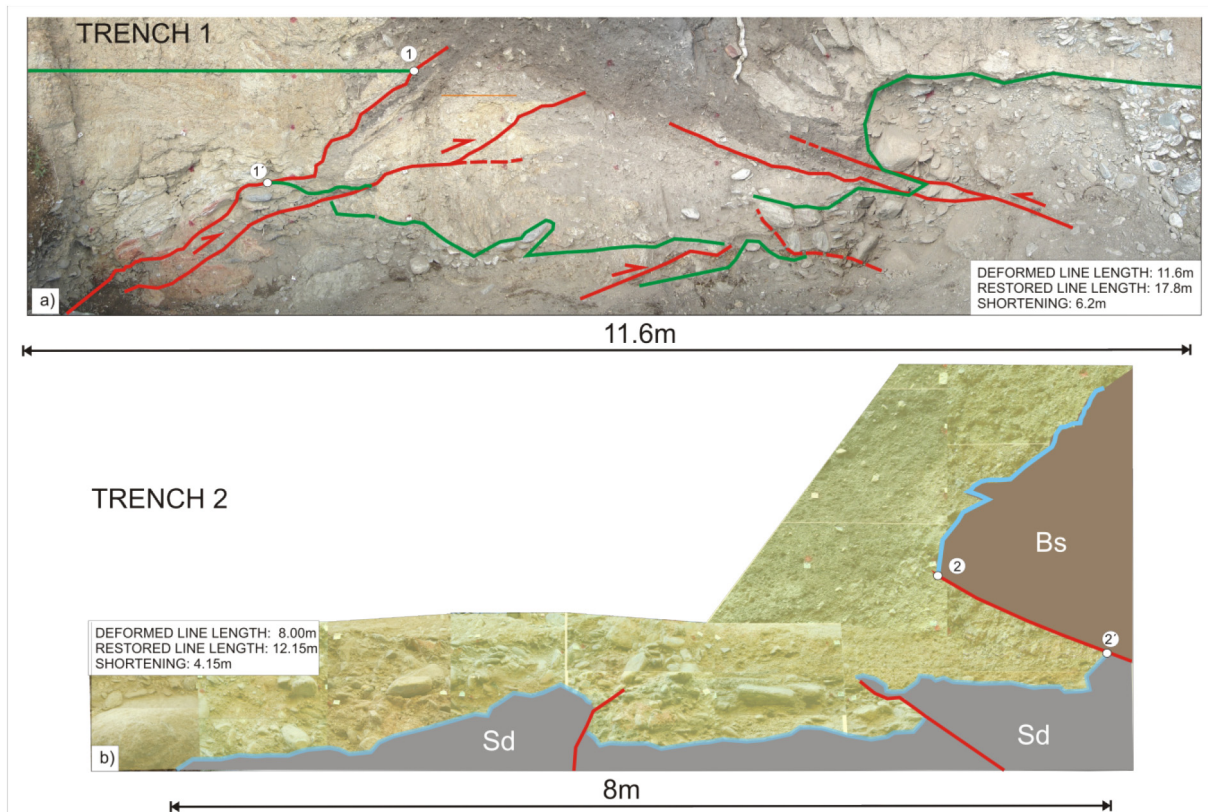
Fig. 11. Different scenarios considered for assessing possible maximum and minimum shortening. a) Top of unit 50 is used as a strain marker. Points 1 and 1′ are here considered as piercing-points with the projected top of unit 50 (green line), constraining the displacement that is interpreted to have taken place along fault F1 after unit 50 deposition. Top of package 5 gravels is considered to be repeated by thrusting. b) Shortening estimated through the restoration of the erosion surface at the top of bedrock (trench 2), assumed to be flat before the deposition of package 5. Points 2 and 2′ are considered to have been adjacent to the fault surface before gravel deposition. More details in the text. (For interpretation of the references to color in this figure legend, the reader is referred to the web version of this article.)

Assuming that points 2 and 2′ were adjacent right before deposition of unit 51 (Fig. 11b), this suggests 4.15 m of shortening.

The maximum shortening value obtained (6.2 m) was combined with the minimum age of unit 50 (6.4 ka) to assess the maximum shortening rate. The minimum shortening rate was determined by relating the minimum shortening (4.15 m) with the maximum age of unit 50 (7.8 ka), assuming that deposition of package 5 took place over a short time period. These yield 0.53 and 0.97 mm/a for minimum and maximum shortening rates, respectively, with a mean shortening rate of 0.7 ± 0.2 mm/a (Table 4).

The stratigraphic markers used define only apparent displacements because trench 1 is not perpendicular to fault traces and as such the true dip-slip component is not properly captured. Likewise, the strike-slip component is a significant component in the total slip vector (Fig. 6c). Thus, a three-dimensional strain marker is needed for a more exact estimation of the cumulative deformation.

6. Conclusions

The deformation zone along the El Molino fault exposes complex geometry and evidence of coseismic surface deformation during the past ~7 ka related to the interaction of opposite-verging thrusts. A minimum of three surface deformation events has been recorded in the stratigraphy, suggesting coseismic slip of ~1 m for some of the rupture events. Our estimated shortening rate of 0.7 ± 0.2 mm/a, although derived from incomplete evidence, is not discordant with the overall evidence of deformation.

GPS velocity vectors suggest an elastic shortening rate of 2–4 mm/a at the Andean orogenic front, which abruptly decreases across the Sierras Pampeanas («1 mm/a) (Kendrick et al., 1999, 2006; Brooks et al., 2003). The deformation evident in the Holocene deposits, the number of rupture events identified and the estimated shortening rates, suggest that surface deformation related to crustal seismicity is more significant than predicted by both GPS-derived deformation rates and the seismic catalog, at least in terms of frequency and magnitude of morphogenic earthquakes. Shortening rates estimated at the El Molino fault (700 km away from the subduction zone) are similar to some Andean frontal thrusts (~1 mm/a) (see Costa et al., 2015 for a review) and are near one order of magnitude higher than those suggested by tectonic geodesy and the Quaternary shortening rates for neighboring structures (Sagripanti and Villalba, 2011; Costa et al., 2014).

As for surface rupture repeatability, if adopting the interpretation of nine deformation events over the past ~7 ka have occurred in this tectonic setting, then the data collected suggest a burst of fault activity with associated surface deformation. If instead the cumulated deformation was driven by few (~3) rupture events, then it should be considered that surface ruptures associated with magnitudes > 7 are possible with a recurrence of 2–3 ka. The historic seismic catalog for this region records no surface displacements related to crustal earthquakes of $M_w \leq 7.4$. Primary coseismic ruptures documented in our study account for a primary coseismic slip of ~1 m, which according to most empirical relationships, should be associated with prehistoric earthquakes of $M_w \geq 6.6$. This interpretation differs from the maximum magnitudes recorded by the seismic record ($M_s \leq 6.5$ for the Córdoba and San Luis Ranges). In our interpretation, $M_w \geq 7.0$ corresponds to the threshold magnitude for crustal earthquakes to produce ground deformation in this tectonic setting. Thus, documentation of surface ruptures and their seismogenic parameters, in the Quaternary stratigraphic record, even if poorly defined, adds relevant data to the seismic catalog of this region currently experiencing low to moderate seismicity.

Paleoseismic magnitude estimates according to worldwide empirical relationships based on rupture length and rupture area, result in magnitudes lower than threshold values for surface deformation in the Sierras Pampeanas (INPRES, 1977). This would lead to the interpretation that the El Molino fault is not capable of producing earthquakes with an associated surface rupture, which would result in underestimation of the seismic potential of these structures. There are very few crustal settings worldwide with which to compare the geomorphic signature, seismogenic parameters and seismic capability of the active Quaternary structures at this study site. Therefore, caution is needed when estimating magnitudes for paleoseismic events using the main parameters in most accepted empirical relationships.

References

Adamiec, G., Aitken, M., 1998. Dose-rate conversion factors: update. Ancient TL 16, 37–50.

Alvarado, P., Beck, S., 2006. Source characterization of the San Juan (Argentina) crustal earthquakes of 15 January 1944 (Mw 7.0) and 11 June 1952 (Mw 6.8). Earth Planet. Sci. Lett. 243, 615–631. http://dx.doi.org/10.1016/j.epsl.2006.01.015.

Anderson, J., Wesnousky, S., Stirling, M., 1996. Earthquake size as a function of fault slip rate. Bull. Seismol. Soc. Am. 86 (3), 683–690.

Baize, S., McCalpin, J., Scotti, O., Costa, C., Cinti, F., Michetti, A., Okumura, K., Dawson, T., 2015. Earthquake geology of shallow crustal faults and Seismic Hazard Assessment: challenges ahead. In: 6th International INQUA Meeting on Paleoseismology, Active Tectonics and Archaeoseismology, INGV Miscellanea 27, pp. 92–95 (ISSN 2039-6651).

Berryman, K., Villamor, P., 2004. Surface rupture of the Poulter Fault in the 1929 March 9 Arthurs Pass earthquake, and redefinition of the Kakapo Fault. N. Z. J. Geol. Geophys. 47, 341–351.

Biasi, G., Weldon II, R., 2006. Estimating surface rupture length and magnitude of paleoearthquakes from point measurements of rupture displacement. Bull. Seismol. Soc. Am. 96, 1612–1623.

Brooks, B., Bevis, M., Smalley Jr., R., Kendrick, E., Manceda, R., Lauría, E., Maturana, R., Araujo, M., 2003. Crustal motion in the Southern Andes (26°–36°S): do the Andes behave like a microplate? Geochem. Geophys. Geosyst. 4 (10). http://dx.doi.org/10.1029/2003GC000505.

Bull, W., 2007. Tectonic Geomorphology of Mountains: A New Approach to Paleoseismology. Blackwell Publishing Ltd. (ISBN-13: 978-1-4051-5479-6).

Clark, D., McPherson, A., Allen, T., De Kool, P., 2014. Coseismic surface deformation caused by the 23 March 2012 Mw 5.4 Ernabella (Pukatja) earthquake, central Australia: implications for fault scaling relations in Cratonic settings. Bull. Seismol. Soc. Am. 104 (1). http://dx.doi.org/10.1785/0120120361.

Costa, C., 1996. Análisis neotectónico en las Sierras de San Luis y Comechingones: Problemas y métodos. In: Paper Presented at13rd Congreso Geológico Argentino, Actas 2: 285–300. Buenos Aires, Argentina.

Costa, C., 1999. Tectónica Cuaternaria en las Sierras Pampeanas. In: Caminos, R. (Ed.), Geología Argentina, pp. 779–784 (Anales 29 (24), Sección 2B, SEGEMAR, Buenos Aires).

Costa, C., 2005. The seismogenic potential for large earthquakes at the southernmost Pampean flat-slab (Argentina) from a geologic perspective. In: Paper Presented at 5th International Symposium on Andean Geodynamics: 211–214, Barcelona.

Costa, C., Morla, P., 1996. Algunos rasgos estructurales de la depresión del río Conlara, provincias de San Luis y Córdoba. In: Paper Presented at 13th Congreso Geológico Argentino, Actas 2: 283. Buenos Aires.

Costa, C., Vita Finzi, C., 1996. Late Holocene faulting in the Southeast Sierras Pampeanas of Argentina. Geology 24 (12), 1127–1130.

Costa, C., Murillo, M., Vita-Finzi, C., Gardini, C., 1994. Quaternary faulting and perspectives for paleoseismological studies in the southeastern Pampean Ranges, Argentina. In: Prentice, C., Schwartz, D., Yeats, R. (Eds.), Workshop on Paleoseismology: United States Geological Survey Open-File Report 94-568, pp. 39–40.

Costa, C., Cesco, J., Morán, R., 1997. A simple graphical method for estimating the components of the fault-slip vector. J. Struct. Geol. 19, 1245–1247.

Costa, C., Ortiz Suárez, A., Gardini, C., Chiesa, J., Ojeda, G., Strasser, E., Escayola, M., Kraemer, P., Ulacco, H., Morla, P., Almandoz, G., Coniglio, J., 1998. Hoja Geológica 3366-II, Santa Rosa, provincias de San Luis y Córdoba, Escala 1:250.000. SEGEMAR, Boletín 373, Buenos Aires.

Costa, C., Murillo, V., Sagripanti, G., Gardini, C., 2001. Quaternary intrapalate deformation in the southeastern Sierras Pampeanas, Argentina. J. Seismol. 5, 399–409.

Costa, C., Massabie, A., Sagripanti, G., Brunetto, E., Coppolecchia, M., 2014. Neotectónica de la provincia de Córdoba. In: Martino, R., Guereschi, A. (Eds.), Relatorio del XIX

Congreso Geológico Argentino. Asoc. Geol. Arg., pp. 725–748.

Costa, C., Ahumada, E., Vazquez, F., Kröhling, D., 2015. Holocene shortening rates of an Andean-front thrust, Southern Precordillera, Argentina. Tectonophysics 664, 191–201. http://dx.doi.org/10.1016/j.tecto.2015.09.017.

Crone, A., Machette, M., Bowman, J., 1997. Episodic nature of earthquake activity in stable continental regions revealed by palaeoseismicity studies of Australian and North American Quaternary faults. Aust. J. Earth Sci. 44, 203–214.

González Bonorino, F., 1950. Algunos problemas geológicos de las Sierras Pampeanas. Rev. Asoc. Geol. Argent. 16 (1–2), 61–106.

González Díaz, E., Fauqué, L., Giaccardi, A., Costa, C., Pereyra, F., Palomera, R., 1997. La avalancha de rocas de Potrero de Leyes, Oeste de la Sierra de San Luis. Rev. Asoc. Geol. Argent. 52, 93–107.

González Díaz, E. Fauqué, Costa, C., Giaccardi, A., 1998. La avalancha de rocas de Las Cañas: Otra manifestación de estos fenómenos en la sierra Grande de San Luis. Rev. Asoc. Geol. Argent. 53, 325–336.

Grützner, C., Carson, E., Walker, R., Rhodes, E., Mukambayev, A., Mackenzie, D., Elliott, J., Campbell, G., Abdrakhmatov, K., 2017. Assessing the activity of faults in continental interiors: palaeoseismic insights from SE Kazakhstan. Earth Planet. Sci. Lett. 459, 93–104. http://dx.doi.org/10.1016/j.epsl.2016.11.025.

Gutscher, M.A., Spakman, W., Bijwaard, H., Engdahl, E., 2000. Geodynamics of flat subduction: seismicity and tomographic constraints from the Andean margin. Tectonics 19, 814–833. http://dx.doi.org/10.1029/1999TC001152.

Hermanns, R., Strecker, M., 1999. Structural and lithologic controls on large Quaternary rock avalanches (Sturzstroms) in arid Northwestern Argentina. Geol. Soc. Am. Bull. 11, 934–948.

Ikeda, Y., 1983. Thrust-front migration and its mechanism: evolution of intraplate thrust fault systems. In: Bulletin of the Department of Geography. 15. University of Tokyo, pp. 125–159.

INA-CRAS, 2004. Estudio de fuentes de abastecimiento de agua potable a la Villa de Merlo, departamento Junin, provincia de San Luis, Technical Report IT-228, 204p, San Juan.

INPRES, 1977. Zonificación sísmica de la República Argentina, Publicación Técnica 5, 42p., San Juan.

Jordan, T., Allmendinger, R., 1986. The Sierras Pampeanas of Argentina: a modern analogue of Rocky Mountain foreland deformation. Am. J. Sci. 286 (10), 737–764.

Jordan, T., Isacks, B., Allmendinger, R., Brewer, J., Ramos, V., Ando, C., 1983. Andean tectonics related to geometry of subducted Nazca plate. Geol. Soc. Am. Bull. 94 (3), 341–361.

Kadinsky-Cade, K., Reilinger, R., Isacks, B., 1985. Surface deformation associated with the November 23, 1977, Caucete, Argentina, earthquake sequence. J. Geophys. Res. 90, 12691–12700.

Kay, S., Mpodozis, C., Ramos, V., Munizaga, F., 1991. Magma source variations for mid-late Tertiary magmatic rocks associated with a shallowing subduction zone and thickening crust in the Central Andes (28°–33°S). In: Harmon, R.S., Rapela, C.W. (Eds.), Andean Magmatism and Its Tectonic Setting. Geological Society of America Special Paper 26, pp. 113–127.

Kendrick, E., Bevis, M., Smalley Jr., R., Cifuentes, O., Galbán, F., 1999. Current rates of convergence across the Central Andes; estimates from continuous GPS observations. Geophys. Res. Lett. 26, 541–544.

Kendrick, E., Brooks, B.A., Bevis, M., Smalley Jr., R., Lauría, E., Araujo, M., Parra, H., 2006. Active orogeny of the South-Central Andes studied with GPS geodesy. Rev. Asoc. Geol. Argent. 61, 555–566.

Landgraf, A., Kübler, S., Hintersberger, E., Stein, S., 2017. Seismicity, fault rupture and earthquake hazards in slowly deforming regions. Geol. Soc. Lond., Spec. Publ. 432, 1–12. http://dx.doi.org/10.1144/SP432.13.

Langer, C., Hartzell, S., 1996. Rupture distribution of the 1977 western Argentina earthquake. Phys. Earth Planet. Inter. 94, 121–132.

Leonard, M., 2010. Earthquake fault scaling: relating rupture length, width, average displacement, and moment release. Bull. Seismol. Soc. Am. 100 (5A), 1971–1988.

Lettis, W., Wells, D., Baldwin, J., 1997. Empirical observations regarding reverse earthquakes, blind thrust faults, and quaternary deformation: are blind thrust faults truly blind? Bull. Seismol. Soc. Am. 87 (5), 1171–1198.

Löbens, S., Bense, F., Wemmer, K., Dunkl, I., Costa, C., Layer, P., Siegesmund, S., 2011. Exhumation and uplift of the Sierras Pampeanas: preliminary implications of K-Ar fault gouge dating and low thermal geochronology in the Sierra de Comechingones (Argentina). Int. J. Earth Sci. 100 (2–3), 671–694. http://dx.doi.org/10.1007/s00531-010-0608-0.

Martino, R., Guereschi, A., Carignano, C., 2012. Influencia de la tectónica preandina sobre la tectónica andina: el caso de la falla de la Sierra chica, sierras pampeanas de Córdoba. Rev. Asoc. Geol. Argent. 69 (2), 207–221 (Buenos Aires).

Martino, R., Guereschi, A., Caro Montero, A., 2016. Reactivation, inversion and basement faulting and thrusting in the Sierras Pampeanas of Córdoba (Argentina) during Andean flat-slab deformation. Geol. Mag. 153 (5–6), 962–991. http://dx.doi.org/10.1017/S0016756816000339.

McCalpin, J. (Ed.), 2009. Paleoseismology, 2nd Ed. Academic Press, Amsterdam.

McCalpin, J., 2011. Changing direction in paleoseismology: where are faults in their current seismic cycle? In: Paper Presented at 43rd Symposium on Engineering Geology and Geotechnical Engineering, Water, Soils and Sustainability in the Intermountain West, Las Vegas, Nevada, USA, pp. 203–2018.

McCalpin, J., Carver, G., 2009. Paleoseismology of compressional tectonic environments. In: McCalpin, J. (Ed.), Paleoseismology, 2nd ed. Academic Press, Amsterdam.

Mejdahl, V., 1979. Thermoluminescence dating: beta-dose attenuation in quartz grains. Archaeometry 21, 61–72.

Mingorance, F., 1991. Análisis y evaluación del tectonismo reciente asociado a la falla Sampacho, Provincia de Córdoba, Argentina Central. Revista Instituto Panamericano de Geofísica e Historia 35, 13–39 (México).

Murillo, M., 1996. Neotectónica del flanco occidental de la sierra de Comechingones, entre los arroyos Piedra Blanca y San Miguel (Provincia de San Luis). In: Licenciatura Thesis. Universidad Nacional de Buenos Aires, Buenos Aires, pp. 135.

Murray, A.S., Wintle, A.G., 2000. Luminescence dating of quartz using an improved single-aliquot regenerative-dose protocol. Radiat. Meas. 32, 57–73.

Nelson, A., 1992. Lithofacies analysis of colluvial sediments—an aid in interpreting the Recent history of Quaternary normal faults in the Basin and Range Province, Western United States. J. Sediment. Petrol. 62 (4), 607–621. http://dx.doi.org/10.1306/D426796F-2B26-11D7-8648000102C1865D.

Penna, I., Abellán, A., Humair, F., Jaboyedoff, M., Daicz, S., Fauqué, L., 2016. The role of tectonic deformation on rock avalanche occurrence in the Pampeanas Ranges, Argentina. Geomorphology. http://dx.doi.org/10.1016/j.geomorph.2016.07.006.

Prescott, J.R., Hutton, J.T., 1994. Cosmic ray contributions to dose rates for luminescence and ESR dating: large depths and long-term time variations. Radiat. Meas. 23, 497–500.

Rajendran, K., Rajendran, C., Thakkar, M., Tuttle, M., 2001. The 2001 Kutch (Bhuj) earthquake: coseismic surface features and their significance. Curr. Sci. 80, 1387–1405.

Ramos, V., 1988. The tectonics of the Central Andes; 30° to 33°S latitude. In: Clark, S., Burchfiel, C. (Eds.), Processes in Continental Lithospheric Deformation. Geological Society of America Special Paper. 218. pp. 31–54.

Ramos, V., 2009. Anatomy and global context of the Andes: main geologic features and the Andean orogenic cycle. In: Kay, S., Ramos, V., Dickinson, W. (Eds.), Backbone of the Americas: Shallow Subduction, Plateau Uplift, and Ridge and Terrane Collision, Geological Society of America Memoir 204, pp. 31–65.

Ramos, V., Cristallini, E., Pérez, D., 2002. The Pampean flat-slab of the central Andes. J. S. Am. Earth Sci. 15, 59–78.

Staff, R.A., 2013. In: Reimer, P.J., Bard, E., Bayliss, A., Beck, J.W., Blackwell, P.G., Bronk Ramsey, C., Buck, C.E., Cheng, H., Edwards, R.L., Friedrich, M., Grootes, P.M., Guilderson, T.P., Haflidason, H., Hajdas, I., Hatté, C., Heaton, T.J., Hoffmann, D.L., Hogg, A.G., Hughen, K.A., Kaiser, K.F., Kromer, B., Manning, S.W., Niu, M., Reimer, R.W., Richards, D.A., Scott, E.M., Southon, J.R., Turney, C.S.M., Plicht, J.V.D., Reimer, P.J. (Eds.), Radiocarbon. 55, 4. pp. 1869–1887. http://dx.doi.org/10.2458/azu_js.rc.55.16947.

Richardson, T., Gilbert, H., Anderson, M., Ridgway, K., 2012. Geodynamics and tectonics seismicity within the actively deforming Eastern Sierras Pampeanas, Argentina. Geophys. J. Int. 188, 408–420. http://dx.doi.org/10.1111/j.1365-246X.2011.05283.

Sagripanti, G., Villalba, D., 2009. Paleosismicidad y estimación del intervalo de recurrencia de fuertes terremotos asociados a fallas de intraplaca a la latitud de 33° S: Falla Las Lagunas, Sampacho, Córdoba. Rev. Asoc. Geol. Argent. 65 (3), 417–428.

Sagripanti, G., Villalba, D., 2011. Movimientos prehistóricos y recientes en la intraplaca argentina a la latitud 33° S, falla Las Lagunas, Sampacho, Córdoba. Rev. Asoc. Geol. Argent. 68 (4), 491–501.

Schmidt, C., Astini, R., Costa, C., Gardini, C., Kraemer, P., 1995. Cretaceous rifting, alluvial fan sedimentation, and Neogene inversion, Southern Sierras Pampeanas, Argentina. In: Tankard, A., Suarez, R., Helsink, H. (Eds.), Petroleum Basins of South America. 62. Am. Assoc. Petrol. Geol. Mem., pp. 341–358.

Stirling, M., Rhoades, D., Berryman, K., 2002. Comparison of earthquake scaling relations derived from data of the instrumental and preinstrumental era. Bull. Seismol. Soc. Am. 92, 812–830.

Stirling, M., Goded, T., Berryman, K., Lichtfield, N., 2013. Selection of earthquake scaling relationships for Seismic-Hazard Analysis. Bull. Seismol. Soc. Am. 103, 2993–3011. http://dx.doi.org/10.1785/0120130052.

Thompson, J., Burbank, D., Li, T., Chen, J., Bookhagen, B., 2015. Late Miocene northward propagation of the northeast Pamir thrust system, northwest China. Tectonics 34, 510–534. http://dx.doi.org/10.1002/2014TC003690.

Walker, R., Jackson, J., Baker, C., 2003. Surface expression of thrust faulting in eastern Iran: source parameters and surface deformation of the 1978 Tabas and 1968 Ferdows earthquake sequences. Geophys. J. Int. 152, 749–765.

Wells, D., Coppersmith, K., 1994. Empirical relationships among magnitude, rupture length, rupture area, and surface displacement. Bull. Seismol. Soc. Am. 84, 974–1002.

Wesnousky, S., 2008. Displacement and geometrical characteristics of earthquake surface ruptures: issues and implications for seismic-hazard analysis and the process of earthquake rupture. Bull. Seismol. Soc. Am. 98 (4), 1609–1632.

Wesnousky, S., Scholz, C., Shimazaki, K., Matsuda, T., 1984. Integration of geological and seismological data for the analysis of seismic hazard: a case study of Japan. Bull. Seismol. Soc. Am. 74, 687–708.

Yáñez, G., Ranero, C., von Huene, R., Díaz, J., 2001. Magnetic anomaly interpretation across the southern Central Andes (32°–33.5° S): the role of the Juan Fernández ridge in the late Tertiary evolution of the margin. J. Geophys. Res. 106, 6325–6345.